European **J**ournal of **Chem**istry

Check for updates

Synthesis and structural depiction of the isomeric benzimidazole pair and its *in-silico* anti-SARS-CoV-2 activities

Ananya Debnath [1], Shreya Mahato [1], Abhranil De [2], Himanshu Verma [3], Om Silakari [3] and Bhaskar Biswas [1,*]

[1] Department of Chemistry, University of North Bengal, Darjeeling, 734013, India
[2] Department of Basic Science and Humanities, Hooghly Engineering and Technology College, Hooghly 712103, India
[3] Molecular Modeling Laboratory, Department of Pharmaceutical Sciences and Drug Research, Punjabi University, Patiala, Punjab 147002, India

* Corresponding author at: Department of Chemistry, University of North Bengal, Darjeeling, 734013, India.
 e-mail: bhaskarbiswas@nbu.ac.in (B. Biswas).

RESEARCH ARTICLE

ABSTRACT

The present work presents a straightforward synthesis, spectroscopic and structural depiction, and *in silico* anti-SARS-CoV-2 activity of an isomeric monosubstituted benzimidazole pair, 2-(1*H*-benzo[d]imidazol-2-yl)-6-methoxyphenol (L_1O) and 4-(1*H*-benzo[d]imidazol-2-yl)-2-methoxyphenol (L_1P). The derivatives were synthesized by a coupling of aromatic aldehydes and *o*-phenylenediamine in ethanol under reflux. Different spectroscopic methods and X-ray structural analysis were employed to characterize the compounds. The crystal structure of L_1O reveals that the *o*-vanillin substituted benzimidazole compound crystallizes in a monoclinic system and adopts a planar geometry. *In silico* anti-SARS-CoV-2 proficiencies of synthetic derivatives were evaluated against the main protease (M^{pro}) and nonstructural proteins (nsp2 and nsp7) of SARS-CoV-2. Molecular docking reveals the binding scores for the L_1O-M^{pro}, L_1O-nsp2 and L_1O-nsp7 complexes as -11.31, -6.06 and -8.13 kcal/mol, respectively, while the binding scores for the L_1P-Mpro, L_1P-nsp2 and L1P-nsp7 complexes as -10.62, -5.09 and -6.91 kcal/mol, respectively, attributing the excellent conformational stability for both the isomeric benzimidazole derivatives.
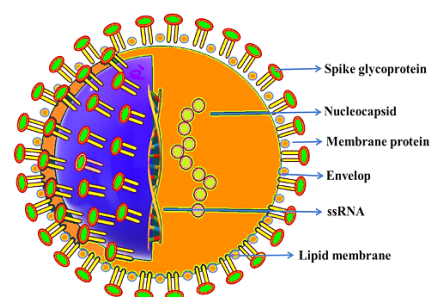
1. Introduction

SARS-CoV-2 shatters the socio-economic status of humans to a great extent [1]. Unprecedented infection by SARS-CoV-2 variants not only severely damages civilization but imposes a significant restriction on scientific development. In particular, 2019-nCoV is a virus of the Coronaviridae family (Scheme 1) and bats are considered a source of development of beta-corona viruses [2-4]. Characteristically, SARS-CoV-2 infection leads to trifling flu into a fatal health emergency [5-9].

Furthermore, SARS-CoV-2 contagion can lead to acute respiratory failure, which ultimately leads to death [10-13]. However, life-threatening issues such as persistent viral load and organ-specific complications, along with compromised antiviral resistance [14,15], are likely to influence the regulation of coronavirus disease. Hence, examination, evaluation, and critical studies of fundamental cellular technologies have gained tremendous attention among the scientific community. In addition to that, synthetic chemists and biologists have made significant efforts in the design and production of molecular therapeutics. Furthermore, the sincere efforts of scientists and health warriors in combating health emergencies are undoubtedly laudable [14,15]. Truly, the immense effort to make significant progress in health and medical science to tackle SARS-CoV-2 infection enforces significant progress to overcome the pandemic instead of the huge population across the globe.

Scheme 1. Schematic diagram of SARS-CoV-2.

Today, the design and production of efficient and cost-effective molecular therapeutics is one of the most challenging

issues to deal with. It is scientifically evidenced that benzimidazole chromophore is potentially utilized in important drugs [16-19]. However, benzimidazole drugs are highly effective against HIV-1 virus [20], hepatitis C virus [21], and act as thrombin inhibitors [22] and antibacterial agents [23]. Recently, our research group has designed and synthesized an indole-substituted benzimidazole and 5-membered hetero-cyclic benzimidazole and explored their SARS-CoV-2 screening activities through computational modeling [24,25]. In this paper, we report the design and synthesis of an isomeric pair of mono-substituted benzimidazoles with their structural charac-terization. Furthermore, anti-SARS-CoV-2 activity against M^{pro}, nsp2 and nsp7 has been explored using *in silico* approaches including molecular docking, electrostatic complementarity, and molecular dynamics.

2. Experimental

2.1. Instrumentations

The FTIR-8400S SHIMADZU spectrometer (Shimadzu, Tokyo, Japan) and the HITACHI U-2910UV-Vis spectrophoto-meter (Hitachi, Tokyo, Japan) were used to record the IR (KBr) and UV-Vis spectra of the isomeric benzimidazoles. NMR spectral analysis was attained on a Bruker Advance 400 MHz instrument. A PerkinElmer 2400 CHN micro analyzer was used to record the elemental analysis. A Rigaku XtaLABmini diffractometer was used to record the X-ray diffraction data, which were reduced using CrysAlisPro 1.171.41.93a and CrysAlisPro 1.171.39.35c [26]. Refinement was performed using the SHELXL-2015 software package [27,28] in the OLEX2 suite [29].

2.2. Synthesis

99.0% *o*-phenylenediamine (Sigma Aldrich, USA), *o*-vanillin (Spectrochem, India), and vanillin (Loba Chemie, India) were obtained and utilized. *o*-Phenylenediamine (0.108 g, 1 mmol) and *o*-vanillin (0.152 g, 1 mmol) / vanillin (0.152 g, 1 mmol) were refluxed separately in ethanol at 80 °C for 8 h. The solutions were evaporated by a rotary evaporator under reduced pressure. A reddish-brown crystalline product for L_1O and a brown gummy mass for L_1P were obtained. The compound L_1O was recrystallized in hot ethanol following a slow evaporation method, while no single crystals were found for L_1P. Both the compounds were stored over $CaCl_2$ for subsequent use.

2-(1H-Benzo[d]imidazol-2-yl)-6-methoxyphenol (**L_1O**): Color: Reddish-brown. Yield: 60.1%. FT-IR (KBr, ν, cm-1): 1640 (C=N, imine), 3428 (O-H, phenolic-OH). ^1H NMR (400 MHz, DMSO-d_6, δ, ppm): 3.82 (t, 3H,CH_3-O), 6.92 (d, *J* = 8.0 Hz, 1H, Ar-H), 6.95 (m, *J* = 8.0 Hz, 1H, Ar-H), 7.06 (d, *J* = 10.7Hz, 1H, Ar-H), 7.63 (m, *J* = 8.9, 8.3 Hz, 2H, Ar- H), 7.72 (d, *J* = 6.7 Hz, 2H, Ar- H), 13.195 (s, 1H, benzimidazole-NH), 13.26 (s, 1H, Ph-OH). ^{13}C NMR (400 MHz, DMSO-d_6, δ, ppm): 56.3 (3C, CH_3-O), 111.9 (1C, Ar-C), 114.3 (2C, Ar-C),118.3 (1C, Ar-C), 121.9 (1C, Ar-C), 123.0 (2C, Ar-C), 133.0 (1C, Ar-C),143.7 (2C, Ar-C), 147.8 (1C, Ar-C), 149.0 (1C, Ar-C), 152.3 (1C, benzimidazole-C). Anal. calcd. for $C_{14}H_{12}N_2O_2$: C, 69.99; H, 5.03; N, 11.66. Found: C, 69.75; H, 5.08; N, 11.73%. UV/Vis (CH$_3$OH, λ$_{max}$, nm, (ε)): 249.19 (0.0676), 307.62 (0.1416).

4-(1H-Benzo[d]imidazol-2-yl)-2-methoxyphenol (**L_1P**): Color: Brown. Yield: 64.8%. FT-IR (KBr, ν, cm-1): 1638 (C=N, imine), 3429 (N-H, phenolic-OH). ^1H NMR (400 MHz, DMSO-d_6, δ, ppm): 3.80 (t, 3H, CH_3-O), 6.91 (d, *J* = 8.1, 4.5 Hz, 1H, Ar-H), 7.15 (d, *J* = 5.3 Hz, 2H, Ar-H), 7.48 (s, 1H, Ar-H), 7.60 (m, *J* = 8.1, 1.9 Hz, 2H, Ar-H), 7.73 (d, *J* = 1.7 Hz, 1H, Ar- H), 9.52 (s, 1H, benzimidazole-NH), 12.64 (s, 1H, Ph-OH). ^{13}C NMR (400 MHz, DMSO-d_6, δ, ppm): 56.1 (3C, CH_3-O), 110.7 (1C, Ar-C), 116.7 (2C,

Ar-C), 120.0 (1C, Ar-C), 121.7 (3C, Ar-C), 122.1 (1C, Ar-C), 148.2 (2C, Ar-C), 148.8 (2C, Ar-C), 152.2 (1C, benzimidazole-C). Anal. calcd. for $C_{14}H_{12}N_2O_2$: C, 69.99; H, 5.03; N, 11.66. Found: C, 69.75; H, 5.08; N, 11.73%. UV/Vis (CH$_3$OH, λ$_{max}$, nm, (ε)): 248.98 (0.0742), 309.67 (0.2075).

2.3. In silico SARS-CoV-2 screening activity

The isomeric benzimidazole pair L_1O and L_1P was analyzed for its potential to act as anti-SARs-CoV2 agents using some *in silico* approaches, including molecular docking electrostatic complementarity, and molecular dynamics studies. Details of protein and ligand preparation, molecular docking study, and are described below [30-33].

2.3.1. Modifications to the protein and ligand for in silico study

The crystal structure described here was generated using the 'Flare protein preparation' plugin (Flare version 4.0) available with Flare module of Cresset software (https://www.cresset-group.com/software/flare/). During this protein preparation, the bond order of co-crystallized ligands was finalized, solvent/water molecules were eliminated, and missing side chains and loops were constructed. Hydrogen atoms were added to the entire protein complex. Subsequently, the preprocessed, optimized, and minimized 3D structure of ALDH1A1 was used for docking analysis. The L_1O / L_1P isomeric ligands were prepared using the 'Flare Ligand preparation' plugin (Flare version 4.0) available with Flare module of Cresset software (https://www.cresset-group.com/software/flare/).

2.3.2. Molecular docking

The molecular docking studies were performed using one of the modules of Cresset Software (https://www.cresset-group.com/software/flare/) *i.e.*, 'Flare'. Initially, the grid was built around the active site. The docking analysis was conducted in a highly accurate but slow mode. The obtained docking results included Rank, dG, and VS scores [24]. Meanwhile, dG and VS scores were optimized to offer accurate estimations of protein-ligand binding energy and maximum efficiency in *in-silico* based screening experiments, respectively [34].

2.3.3. Electrostatic complementarity

Non-covalent interactions such as H-bonding, lone-pair sigma hole (halogen bonding), cation-π, ionic, π-π, and fluorine bonding (orthogonal multipolar interactions) are the major contributors to an effective binding between a drug and target protein. These noncovalent interactions play a crucial role in determining the binding free energy (ΔG) [35]. To calculate the value of ΔG and further assess the match between the isomeric forms L_1O/L_1P and key residues of target proteins in terms of electrostatics, electrostatic complementarity analysis was performed using the Cresset software Flare module (https://www.cresset-group.com/software/flare/). This analysis offered profound insights into how these isoforms bind to each of the three targets connected with SARS-CoV-2 [24].

2.3.4. Molecular dynamics study

The docked complexes harboring the highest docking scores were chosen for subsequent molecular dynamic simulations lasting 50 ns. To execute the dynamic simulations, the 'dynamic' option available with the Cresset software Flare module (https://www.cresset-group.com/software/flare/) was explored. Herein, the AMBER force field [36] and GAFF2
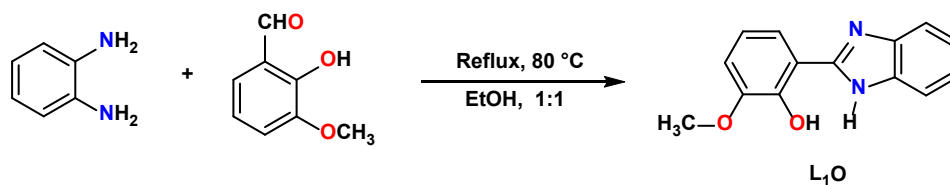
Scheme 2. Synthesis pathway for benzimidazole, L₁O.
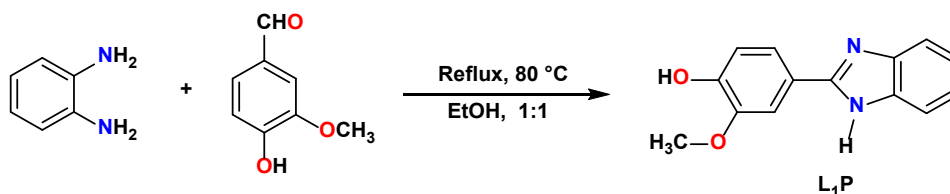
Scheme 3. Synthesis pathway for benzimidazole, L₁P.

[36] options were selected. While AM1-BCC [37] was set as the charge method and a TIP3P solvent system [38] surrounding the complex with $10\times10\times10$ Å dimensions was built. Subsequently, the constructed system underwent a 200ps equilibration using a time step of 2fs. [39]. Following system equilibration, MD simulations lasting 50 ns were executed on a GPU Nvidia Tesla V100, with 16 GB of memory.

2.3.5. Computational analysis

The structural characterization of L₁O and L₁P was also justified with a detailed quantum chemical computation using the Gaussian 09W program suite [40] without considering any symmetrical restrictions. The molecular structures of L₁O and L₁P were optimized in a vacuum adopting the B3LYP theoretical model and 6-311G basis set [41,42].

3. Results and discussion

3.1. Synthesis

The isomeric benzimidazole derivatives were synthesized by adopting a straightforward preparative method through a condensation between o-phenylenediamine and isomeric benzaldehydes in ethanol under reflux. Synthetic procedures are shown in Schemes 2 and 3.

The compounds are soluble in hot water, ethanol, and common polar solvents. We developed single crystals for L₁O using slow evaporation techniques; however, we were unable to produce suitable single crystals for L₁P instead of several trials in hot water, ethanol, water-ethanol, and chloroform-ethanol solvent mixtures. The structural compositions of L₁O and L₁P were examined with various spectral analyzes. The FT IR spectra exhibited the presence of characteristic peaks at 1640 and 1638 cm⁻¹ for L₁O and L₁P, respectively, ascribing the azomethine frequencies. The presence of a broad peak at 3428 and 3429 cm⁻¹ for L₁O and L₁P, respectively, suggests O-H/N-H stretching vibrations. Identified IR frequencies closely align with data reported previously [43,44]. The UV-vis spectra of L₁O and L₁P were obtained in methanol medium. L₁O and L₁P displayed maximum absorption at 230-250 and 305-310 nm. The high energetic bands in the isomeric benzimidazoles provide supporting evidence for the π → π* or n → π* transitions and align with the existing literature [43,44].

The ¹H NMR of the isomeric benzimidazole derivatives was recorded in DMSO-d₆. Aromatic proton signals appeared in the range δ 6.92 to 7.72 ppm for L1O, while the aromatic protons of L₁P displayed their presence between δ 6.89 to 7.73 ppm. The chemical shift value for benzimidazole NH in L₁O and L₁P was obtained at δ 13.195 and 9.526 ppm assigning the -NH protons of the benzimidazole moieties in L₁O and L₁P, respectively, and the peak at δ 3.82-3.87 and 3.83-3.93 ppm represents the methoxy protons of L₁O and L₁P, respectively. Both compounds exhibited signals at δ 13.26 and 12.64 ppm for L₁O and L₁P, respectively, unveiling the -OH protons of the ligands. The ¹³C NMR spectra of L₁O and L₁P were also analyzed, which showed signals at δ 152.38 and 152.25 ppm attributed to the presence of the C atom of benzimidazole, while the characteristic signals at δ 56.29 and 56.10 ppm attributed methoxy-C in the benzimidazoles, L₁O and L₁P, respectively. Aromatic C signals in L₁O and L₁P were detected between δ 111.2-149.0 and 110.7-148.8 ppm, respectively. The reported values of proton and C signals of the benzimidazoles agree well with the literature [45].

3.2. Crystal structure and supramolecular interactions

The X-ray single crystal structural revealed that L₁O crystallizes in a monoclinic crystal system with a *P*2₁/*n* space group. Thermal ellipsoidal plots of L₁O are shown in Figure 1a. The structural parameter is shortened in Table 1 and the bond angles and distances are summarized in Table 2. In L₁O, one methoxy phenol group is connected to the benzimidazole group, adopting a planar structure.

The planarity of the benzimidazole derivative is evident from the measurement of the bond angles between two aromatic moieties, C3-C6-C8 as 178.27°. Furthermore, the bond angles of N1-C8-C6, N2-C8-C6, C5-C6-C8, and C7-C6-C8 are found to be 125.22, 123.45, 122.35, and 118.72°, respectively. The average bond angle, ~122° suggests the high-planarity structure of L₁O. The self-assembled structural analysis of L₁O reveals that methoxyphenol flips 180° to grow a one-dimensional network via close range N···H interactions and moderate-distant O···H interaction in the crystalline phase (Figure 1b). In addition, the 1D chains of L₁O interlink through π···π interactions that build a wonderful supramolecular framework along the *b*-axis (Figure 1c). The noncovalent interaction parameter for L₁O is given in Table 3.

Hirshfeld surface analysis was also performed to understand the interaction propensity of the surface of L₁O. Different surface parameters were also calculated. The surface volume, surface area, globularity, and asphericity were determined as 285.07 Å³, 274.72 Å², 0.762, 0.337, respectively. The 2D fingerprint plots of L₁O were also evaluated. The fingerprint plots show a significant participation of N/O···H hydrogen bonding and π···π interactions as revealed from the sharpness of the tooth. The elemental contribution for 2D fingerprint plots is shown in Table 4.

Table 1. Crystallographic data and structure refinement parameters for L_1O.

Empirical formula	$C_{14}H_{12}N_2O_2$
Formula weight (g/mol)	240.26
Temperature (K)	298.0(2)
Crystal system	Monoclinic
Space group	$P2_1/n$
a, (Å)	7.7190(10)
b, (Å)	12.3492(15)
c, (Å)	12.2568(8)
α (°)	90.00
β (°)	94.138(8)
γ (°)	90.00
Volume (Å³)	1165.3(2)
Z	4
ρ_{calc}(g/cm³)	1.369
μ (mm⁻¹)	0.094
F(000)	504.0
Crystal size (mm³)	0.1 × 0.05 × 0.01
Radiation	MoKα (λ = 0.71073)
2θ range for data collection (°)	6.04 to 54.94
Index ranges	$-8 \leq h \leq 10, -16 \leq k \leq 16, -14 \leq l \leq 15$
Reflections collected	12383
Independent reflections	2646 [R_{int} = 0.0416, R_{sigma} = 0.0315]
Data/restraints/parameters	2646/0/165
Goodness-of-fit on F²	1.034
Final R indexes [I≥2σ (I)]	R_1 = 0.0594, wR_2 = 0.1676
Final R indexes [all data]	R_1 = 0.0879, wR_2 = 0.1980
Largest diff. peak/hole (e.Å⁻³)	0.26/-0.19
CCDC no	2163289
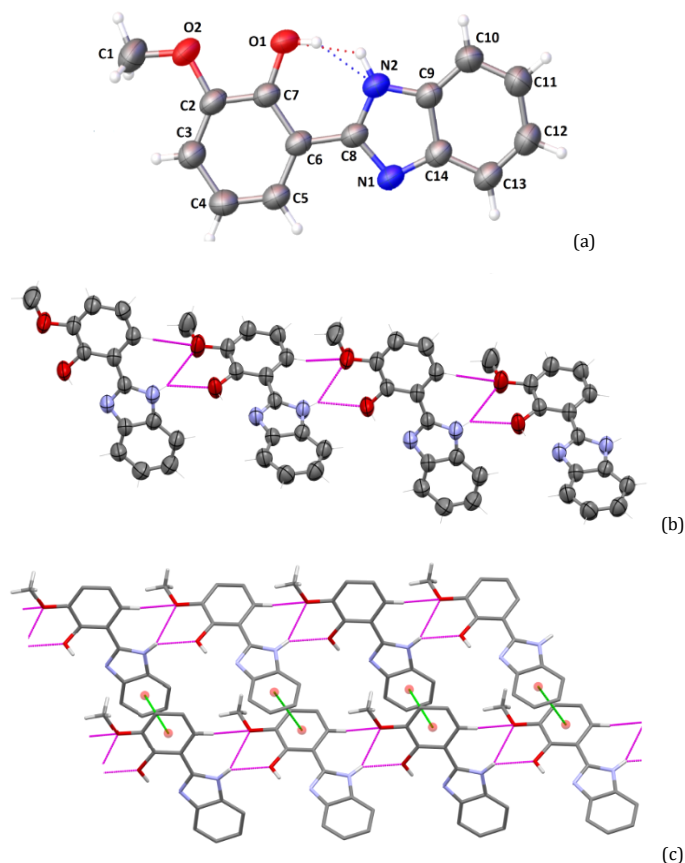
Figure 1. (a) ORTEP diagram of L_1O with 30% probability; (b) Formation of a 1D framework of L_1O based on N···H, O···H hydrogen bonding (pink dotted) along the b axis; (c) Development of the supramolecular 3D crystalline architecture based on π···π interactions.

3.3. Computational outcome

The optimized structure of L_1O showed a good correlation with the crystal structure of L_1O, as evidenced by the closeness of the bond distance and bond angle values (Table 2). Furthermore, the optimization of L_1P reveals the exact structure (Table 5) determined from the spectroscopic analysis. The energy of frontier orbits was also calculated by TD-DFT to understand the electronic properties of the isomeric benzimidazoles, L_1O and L_1P. The energy difference for HOMO and LUMO in L_1O and L_1P displayed values of 4.08 and 4.51 eV, respectively. The closeness of the energy values for the frontier orbitals in L_1O and L_1P is also attributed to the isomeric existence of the compounds.

Table 2. Bond distance and bond angle values of L_1O obtained from XRD and DFT.

Bond distances (Å)					
L_1O	XRD	DFT	L_1O	XRD	DFT
O1-C7	1.354(3)	1.36173	C9-C14	1.404(3)	1.39912
O2-C1	1.419(4)	1.45017	C9-C10	1.382(3)	1.39747
O2-C2	1.372(3)	1.38647	C10-C11	1.371(3)	1.39337
O1-H1	0.8200	1.00825	C11-C12	1.405(3)	1.41060
N1-C8	1.364(3)	1.34159	C12-C13	1.371(3)	1.39550
N1-C14	1.371(3)	1.39527	C13-C14	1.393(3)	1.39527
N2-C9	1.390(3)	1.39912	C1-H1B	0.9600	1.00882
N2-C8	1.325(3)	1.34159	C1-H1C	0.9600	1.09285
N1-H1A	0.8600	1.00298	C1-H1D	0.9600	1.09285
C2-C3	1.367(3)	1.38986	C3-H3	0.9300	1.07941
C2-C7	1.404(3)	1.36173	C4-H4	0.9300	1.08092
C3-C4	1.406(3)	1.40624	C5-H5	0.9300	1.08035
C4-C5	1.365(3)	1.38314	C10-H10	0.9300	1.08035
C5-C6	1.399(3)	1.41404	C11-H11	0.9300	1.08134
C6-C7	1.403(3)	1.36173	C12-H12	0.9300	1.08146
C6-C8	1.460(3)	1.34159	C13-H13	0.9300	1.08156
Bond angles (°)					
L_1O	XRD	DFT	L_1O	XRD	DFT
C1-O2-C2	94.39(11)	118	C10-C11-C12	113.84(9)	121
C7-O1-H1	172.17(11)	109	C11-C12-C13	133.5(2)	121
C8-N1-C14	84.57(15)	108	C12-C13-C14	158.3(2)	116
C8-N2-C9	89.78(3)	106	N1-C14-C13	108.9(3)	132
O2-C2-C7	96.25(10)	115	C9-C14-C13	110.00	122
C3-C2-C7	96.71(12)	120	N1-C14-C9	110.00	105
O2-C2-C3	125.2(2)	124	C4-C5-C6	121.0(2)	120
C2-C3-C4	119.6(2)	120	C7-C6-C8	118.72(18)	118
C3-C4-C5	120.2(2)	120	C5-C6-C7	118.9(2)	119
N1-C8-N2	111.33(19)	110	C5-C6-C8	122.35(19)	122
N2-C8-C6	123.45(18)	123	O1-C7-C2	117.48(19)	118
N1-C8-C6	125.22(18)	125	O1-C7-C6	123.2(2)	122
N2-C9-C14	108.43(19)	109	C2-C7-C6	119.35(19)	119
C10-C9-C14	120.7(2)	120	C9-C10-C11	117.8(2)	117
N2-C9-C10	130.8(2)	130			

Table 3. Intermolecular hydrogen bonding (Å, °) parameter.

D-H···A	D-H	H···A	D···A	∠D-H···A	Symmetry
O1-H1···N2	0.82	1.86	2.595(2)	148	-
N1-H1A···O1	0.86	2.26	3.016(2)	146	1/2+*x*, 1/2-*y*, 1/2+*z*
N1-H1A···O2	0.86	2.49	3.101(2)	129	1/2+*x*, 1/2-*y*, 1/2+*z*
N2-H2···O1	0.86	2.02	2.595(2)	124	-

Table 4. Percentage elemental contribution for Hirshfeld surface.

Inside	Outside	% Surface area included	Inside	Outside	% Surface area included
All	All	100.0	N	All	3.1
All	O	6.9	C	All	22.6
All	H	73.1	C	C	6.3
All	N	2.6	N	H	2.9
All	C	17.4	H	N	2.4
O	All	8.0	O	H	7.6
H	All	66.3	H	O	6.3

3.4. Molecular docking studies

As suggested in the literature [24], Glu 74 and Asp 67 are crucial in inhibiting the biological activity of nsp7 in SARS-CoV2. After the docking simulations, it was observed that both isomeric forms showed strong hydrogen bond interactions with Asp 67. However, the isomeric form of the compound L_1O showed the highest docking scores in terms of the LF rank score (Lead Finder Rank Score), LF dG (Protein-ligand binding energy), LF VS score (Rank-ordering of active and inactive compounds in virtual screening experiments) and LF LE (Estimated ligand efficiency) with values of -8.135, -5.335, -6.574 and -0.296, respectively.

The docking results corresponding to each of the designed molecules with the target nsp7 are displayed in Table 6. The interaction pattern for this compound is shown in Figure 2c. This indicates that L_1O is a potential nsp7 inhibitor. A similar type of observation was disclosed in docking experimentation with the other two targets, *i.e.*, nsp2 and the main protease. As disclosed in Tables 6 and 7, among the designed compounds, only L_1O could manifest the highest docking scores to PDB 7EXM and PDB 6LU7. As observed in Figure 2b, L_1O interacted with crucial residues, *i.e.*, Glu 110 and Lys 113 with additional

hydrogen bonding with Arg 108. In addition to the observed key interactions, this compound also showed good docking scores, as shown in Table 6. The docked complexes of the designed compounds and the main protease protein were also analyzed and it was observed that L_1O not only showed good interactions and docking scores with nsp7 and nsp2 but also showed good interactions with the main protease enzyme (Figure 2a). The best docking scores in comparison to these two proteins were observed with M^{pro} enzyme. As observed in Table 7, L_1O showed -11.311, -7.139, -8.694 and -0.397 values for the LF rank score, the LF dG, the LF VS score and the LF LE. Moreover, they manifested key H-bond interactions with Leu 141, His 163, Gly 143, and Ser 144. From the docking study, it could be concluded that L_1O is the potential multitargeting molecule that can potentially interfere with the normal functioning of nsp7, nsp2 and M^{pro}.

3.5. Electrostatic complementarity analysis

Electrostatic complementarity (EC) analysis for an isomeric form of benzimidazole in a complex with each of the selected anti-SARS-CoV2 targets can provide important insight into the nature and strength of their complexes.

Table 5. Bond distance and bond angle values of L₁P obtained from DFT.

Bond distances (Å)

L₁P	DFT	L₁P	DFT
O11-H12	0.97162	C17-C18	1.33093
O10-C13	1.46809	C17-N19	1.39628
C13-H14	1.08537	N19-H20	1.00293
C13-H15	1.09209	C21-C22	1.39276
C13-H16	1.08620	C22-C23	1.39526
O10-C5	1.39299	C24-C25	1.39272
O11-C6	1.39503	C25-C26	1.39827
C1-C2	1.39451	C26-C21	1.39827
C2-C3	1.40393	C22-H27	1.08187
C3-C4	1.40624	C23-H28	1.08174
C4-C5	1.38917	C24-H29	1.08174
C5-C6	1.39465	C25-H30	1.08041
C3-C17	1.46059	C2-C8	1.08191
C4-H9	1.07900	C1-C7	1.08375
C6-C1	1.39465		

Bond angles (°)

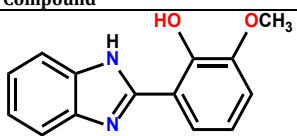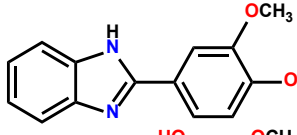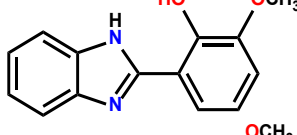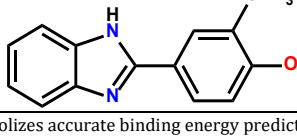| L₁P	DFT	L1P	DFT
C1-O2-C2	118	C10-C11-C12	121
C3-O1-H1	111	C11-C12-C13	121
C8-N1-C14	107	C12-C13-C14	116
C8-N2-C9	106	N1-C14-C13	133
O2-C2-C7	117	C9-C14-C13	122
C3-C2-C7	119	N1-C14-C9	104
O2-C2-C3	122	N2-C9-C10	129
C2-C3-C4	119	C9-C10-C11	118
C3-C4-C5	120	O1-C3-C4	122
C4-C5-C6	120	C2-C7-C6	121
C7-C6-C8	118	N1-C8-N2	111
C5-C6-C7	118	N2-C8-C6	124
C5-C6-C8	122	N1-C8-C6	123
O1-C3-C2	117	N2-C9-C14	109
C10-C9-C14	120		
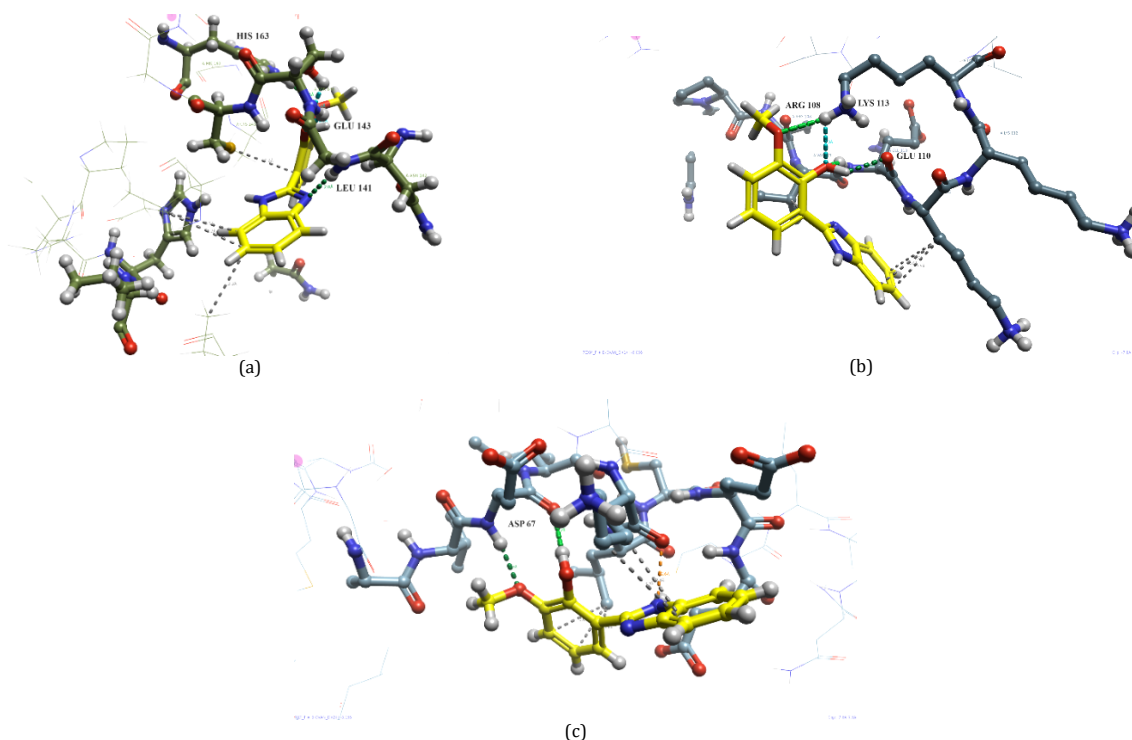
Figure 2. 3D docked poses for L₁O in the active site of (a) main-protease; 6LU7, (b) nsp2; 7EXM, and (c) nsp7; 7JLT.

As discussed in the Material and Methods section that electrostatic interactions are key contributors to the ΔG, EC map of each isomeric form was generated with respect to each selected target. As suggested by the docking analysis, L₁O is a more potential anti-SARs-CoV2 agent compared to L₁P due to its higher docking scores. Electrostatic complementarity analysis also suggested that L₁O exhibits higher complementarity to each of the selected targets, *i.e.*, nsp7, nsp2 and the main protease as revealed by the EC scores displayed in Tables 8 and 9, respectively. It is clear from the EC maps shown in Figures 3-5 that L₁O exhibited higher electrostatic complementarity with the key residues of each selected target.
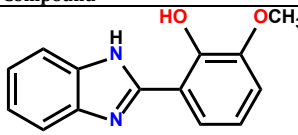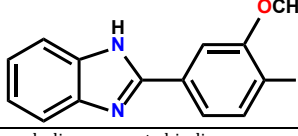
In this paper, the green color suggested electrostatic complementarity, while the red color suggested electrostatic clashes. The highest electrostatic complementarity can be observed in Figure 4 with minimal electrostatic clashes.

Table 6. Docking results for the designed molecules, nsp7 (7JLT) and nsp2 (7EXM) complexes *.

Complex	Compound	LF rank score	LF dG	LF VS score	LF LE	Interactions
nsp7 (7JLT)		-8.135	-5.335	-6.574	-0.296	2-Hydrogen bonding Asp 67
nsp7 (7JLT)		-6.919	-4.869	-5.580	-0.270	3-Hydrogen bonding Asp 67
nsp2 (7EXM)		-6.066	-4.347	-4.728	-0.242	3-Hydrogen bonding Lys 113, Glu 110, Lys 111
nsp2 (7EXM)		-5.009	-3.746	-3.894	-0.208	3-Hydrogen bonding Lys 113, Glu 110

* LF-dG score symbolizes accurate binding energy predictions; LF-VS score indicates correct rank-ordering of active and inactive compounds in virtual screening experiments; LF-Rank score indicates correct energy-ranking of docked ligand poses; LF-LE score signifies estimated ligand efficiency.

Table 7. Docking results for designed molecules and Covid-19 main protease (6LU7) complexes *.

Sample	Compound	LF rank score	LF dG	LF VS score	LF LE	Interactions
L_1O		-11.311	-7.139	-8.694	-0.397	5-Hydrogen bonding His 163, Ser 144 and Gly 143
L_1P		-10.629	-6.327	-7.499	-0.352	2-Hydrogen bonding His 163, Gly 143

* LF-dG score symbolizes accurate binding energy predictions; LF-VS score indicates correct rank-ordering of active and inactive compounds in virtual screening experiments; LF-Rank score indicates correct energy-ranking of docked ligand poses; LF-LE score signifies estimated ligand efficiency.
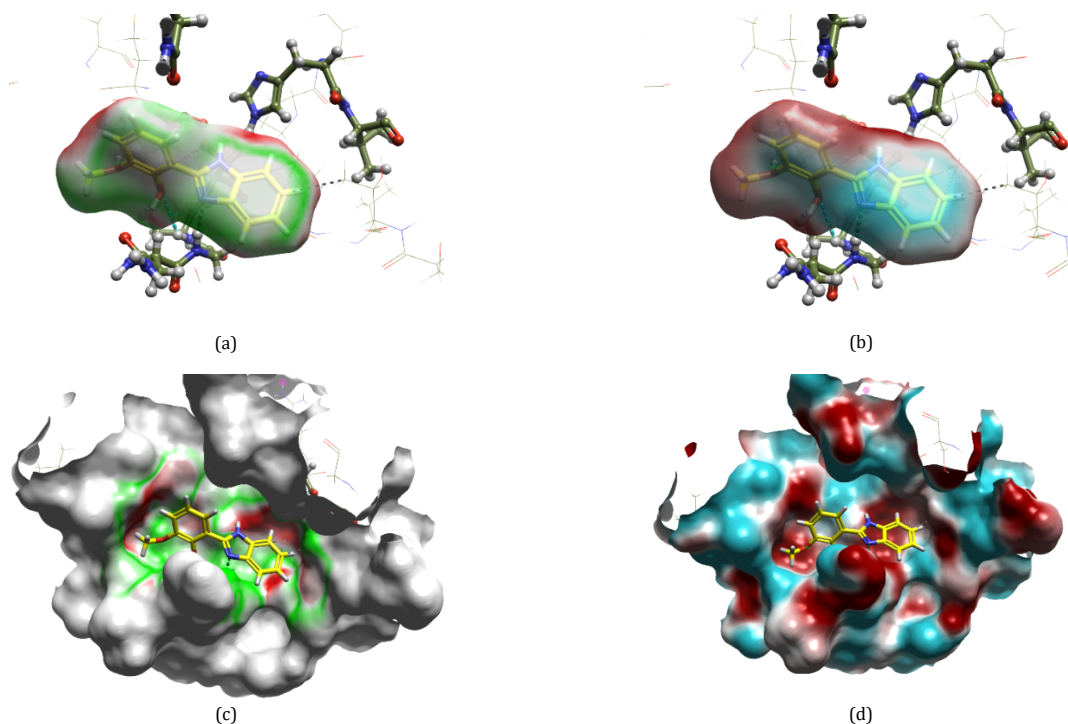

(a)

(b)

(c)

(d)

Figure 3. Electrostatic complementarity analysis for L_1O-main protease complex (a) L_1O EC, (b) L_1O EP, (c) EC with respect to the active site of main protease, (d) EP with respect to the active site of main protease.

Table 8. Electrostatic complementarity analysis results for L_1O, L_1P in complex with nsp7 (PDB ID: 7JLT) and L_1O, L_1P in complex with nsp2 (PDB ID: 7EXM) *.

Compounds	Complex with	EC	EC_r	EC_{rho}
L_1O	nsp7 (PDB ID: 7JLT)	0.28	0.18	0.32
L_1P	nsp7 (PDB ID: 7JLT)	0.20	0.32	0.27
L_1O	nsp2 (PDB ID: 7EXM)	0.39	0.35	0.45
L_1P	nsp2 (PDB ID: 7EXM)	0.20	0.11	0.24

* EC: Electrostatic complementarity (Normalized surface integral of the complementarity score); EC_r: Pearson correlation coefficient of protein and ligand electrostatic potentials sampled on the surface vertices; EC_{rho}: Spearman rank correlation coefficient of protein and ligand electrostatic potentials sampled on the surface vertices.
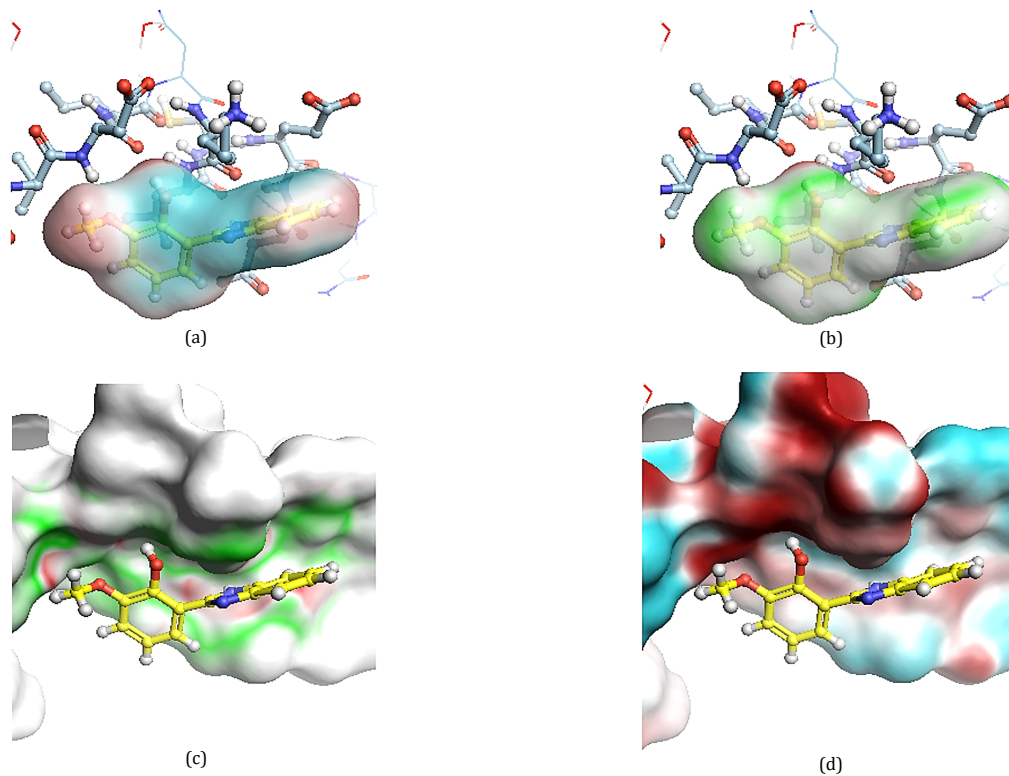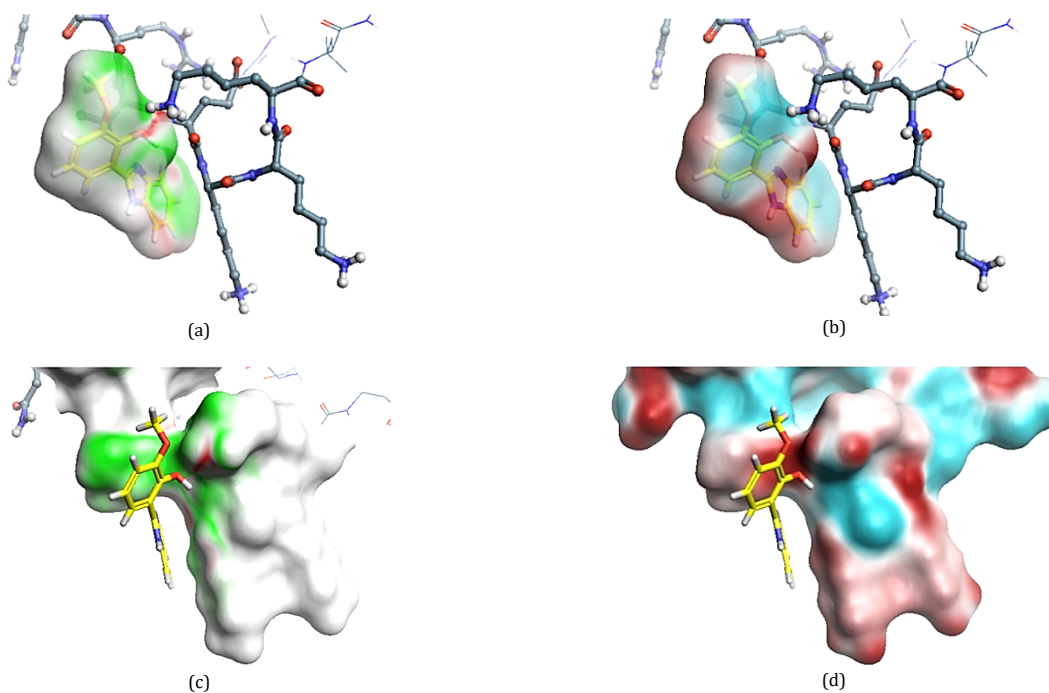

Figure 4. Electrostatic complementarity analysis for L_1O-nsp7 complex (a) L_1O EP, (b) L_1O EC, (c) EC with respect to the active site of nsp7, (d) EP with respect to the active site of nsp7.

Figure 5. Electrostatic complementarity analysis for the L_1O-nsp2 complex (a) L_1O EC, (b) L_1O EP, (c) EC with respect to the active site of the nsp2, and (d) EP with respect to the active site of the nsp2.
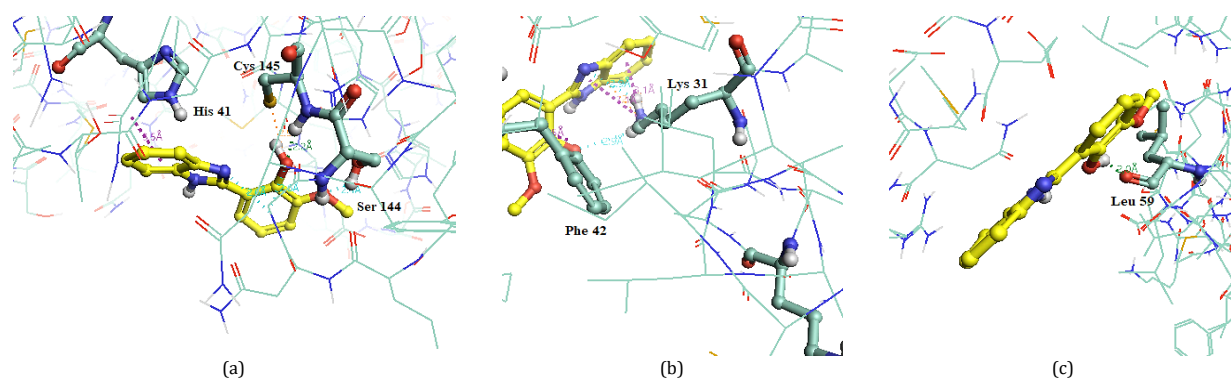
Table 9. Electrostatic complementarity analysis results for the designed ligands with each of the selected targets *.

Compounds	EC	EC_r	EC_{rho}
L_1O	0.24	0.31	0.33
L_1P	0.17	0.10	0.17

* EC: Electrostatic complementarity (Normalized surface integral of the complementarity score); EC_r: Pearson correlation coefficient of protein and ligand electrostatic potentials sampled on the surface vertices; EC_{rho}: Spearman rank correlation coefficient of protein and ligand electrostatic potentials sampled on the surface vertices.

Table 10. Interactions after carrying molecular dynamics for the L_1O and main protease 6LU7 complex.

Bond type	Ligand atom	Protein atom	% Frames present
Hydrogen-bond	B MOL 308 O2	A SER 144 HG	36.5
Aromatic-Aromatic	B MOL 308 C1	A HIS 41 HD2	35.5
Hydrogen bond	B MOL 308 O1	A GLY 143 H	34.6
Hydrogen bond	B MOL 308 O1	A CYS 145 H	26.0
Hydrogen bond	B MOL 308 N1	A GLY 143 H	22.7
Hydrogen bond	B MOL 308 O1	A SER 144 H	11.8
Aromatic-Aromatic	B MOL 308 C4	A HIS 41 NE2	8.2
Aromatic-Aromatic	B MOL 308 C1	A HIS 41 NE2	4.9
Hydrogen bond	B MOL 308 O1	A SER 144 HG	4.7

(a)   (b)   (c)

Figure 6. 3D interaction diagram after MD considering docked complexes (A) L_1O-main protease, (B) nsp2, and (C) nsp7.

Electrostatic complementarity was also observed in the L_1O-main protease complex, very slight electrostatic clashes were observed due to edge aromatic-aromatic interactions between the benzimidazole core in L_1O and the imidazole ring of His 163 (Figures 3a and 3c). From the electrostatic potential (EP) maps displayed in Figures 3b, 3d, 4a, 4d, 5b, and 5d, it can be observed that the negative EP surface of the ligand mapped over the positive EP surface of the protein and vice versa. This marked the relevance of higher complementarity of L_1O with M^{pro}, nsp7 and nsp2.

3.6. Molecular dynamics

The top docking scored L_1O was found to retain its molecular docking interaction with the target M^{pro} even after the molecular dynamic simulation for a period of 50 ns. This compound also shows slightly fewer RMSD (Root Mean Square Deviation) fluctuations in the case of M^{pro} in comparison to the other two proteins, *i.e.,* nsp7 and nsp-2. While prominent RMSD fluctuations were observed in nsp7 and nsp2 indicating that L_1O is a potential inhibitor of M^{pro} in comparison to the other two proteins. Furthermore, the percentage of interactions with key residues Ser 144, Cys 145, Gly 143, and His 41 was observed to be the highest for the same, which can be observed in Table 10. The L_1O was unable to retain the docking interaction in the case of nsp2 and nsp7. In general, it could be concluded that L_1O is a promising molecule that can efficiently inhibit the main protease and prevent the progression of Covid-19 disease.

In the current scenario of SARS-CoV-2 infection around the world, computer-aided structural modification and drug design receive a great deal of attention among scientists [46-48]. Different scientist groups have shown that a promising change of dG Bind energy is a primary necessity (-10 to -100 kcal/mol) for the design of tailor-made therapeutic against M^{pro} and nsp proteins [46-47]. Interestingly, Purwati and his colleagues [48]

rationally designed and evaluated the inhibition activities of a series of dual combinatory drugs such as Lopinavir-Ritonavir-Azithromycin, Lopinavir-Ritonavir-Clarithromycin, Hydroxy-chloroquine-Azithromycin, Lopinavir-Ritonavir-Doxycycline, *etc*. against Vero cell lines. In comparison with the computationally calculated binding scores of the compounds through molecular docking and MD simulation, the synthetic ligand L_1O showed an excellent binding priority with His 163, Gly 143 and Ser 144 of the M^{pro} of SARS-CoV-2 through a significant number of hydrogen bonding while L_1P formed a hydrogen bonding with His 163, Gly 143 but a lesser extent with respect to L_1O as evidenced from the stability of conformations (Figure 6).

4. Conclusions

In summary, we report a straightforward synthetic approach to prepare an isomeric pair of benzimidazole derivatives and characterize them using a range of spectroscopic techniques and X-ray crystallography. Interestingly, the ortho-positioned -OH group to methoxybenzene marks a significant impact on the functional properties relative to the ortho-positioned -OH. The *in silico* SARS-CoV-2 screening activities against M^{pro}, nsp2, and nsp7 were evaluated by molecular docking, electrostatic complementarity study, and MD simulation studies. Molecular docking reveals the binding scores for L_1O-M^{pro}, L_1O-nsp2 and L_1O-nsp7 complexes as -11.31, -6.06 and -8.13 kcal/mol while the binding scores for L_1P-Mpro, L_1P-nsp2 and L_1P-nsp7 complexes as -10.62, -5.09 and -6.91 kcal/mol attributing the stable conformations for both isomeric benzimidazole derivatives. The origin of relatively higher stability of the L_1O-protein docked conformation was enumerated through the larger number of hydrogen bonding formation propensity of L_1O with His 163, Ser 144 and Gly 143 of Mpro relative to that of L_1P. The 50 ns time-framing MD simulation studies for the docked complexes

reveal a similar trend to molecular docking complexes and attribute the significant effect of o-positioned phenolic-OH. The O-positioned OH facilitates a significant number of hydrogen bonding compared to the p-positioned OH, ensuring a more stable conformation of L_1O with the amino acids of SARS-CoV-2. Therefore, the effect of position on the functional group is an important aspect of drug design. However, the straightforward synthetic procedure, high yield with excellent purity, and remarkable pharmacokinetic properties of the tailor-made benzimidazoles may be helpful in designing a potent thera-peutic agent.

Acknowledgements

Supporting information Ⓢ

CCDC-2163289 contains the supplementary crystallographic data for this paper. These data can be obtained free of charge via www.ccdc.cam.ac.uk/data_request/cif, or by e-mailing data_request@ccdc.cam.ac.uk, or by contacting The Cambridge Crystallographic Data Centre, 12 Union Road, Cambridge CB2 1EZ, UK; fax: +44(0)1223-336033.

Disclosure statement Ⓓⓢ

Conflict of interest: The authors declare that they have no conflict of interest.
Author contributions: All authors contributed equally to this work.
Ethical approval: All ethical guidelines have been adhered.
Sample availability: Samples of the compounds are available from the author.

CRediT authorship contribution statement Ⓒⓡ

Conceptualization: Ananya Debnath, Shreya Mahato, Bhaskar Biswas; Methodology: Ananya Debnath, Shreya Mahato; Abhranil De, Himangshu Verma; Software: Ananya Debnath, Abhranil De, Himangshu Verma; Validation: Ananya Debnath, Abhranil De, Himangshu Verma; Formal Analysis: Ananya Debnath, Shreya Mahato; Abhranil De, Himangshu Verma; Investigation: Ananya Debnath, Shreya Mahato; Abhranil De, Himangshu Verma; Resources: Bhaskar Biswas, Om Silakari; Data Curation: Ananya Debnath, Shreya Mahato; Abhranil De, Himangshu Verma; Writing - Original Draft: Bhaskar Biswas, Om Silakari; Writing - Review and Editing: Bhaskar Biswas; Visualization: Bhaskar Biswas, Om Silakari; Funding acquisition: Bhaskar Biswas; Supervision: Bhaskar Biswas.

ORCID Ⓘⓓ and Email ✉

Ananya Debnath
✉ ananyadebnath2@gmail.com
Ⓘⓓ https://orcid.org/0000-0001-9912-1133
Shreya Mahato
✉ shreyachem13@gmail.com
Ⓘⓓ https://orcid.org/0000-0003-2266-9023
Abhranil De
✉ abhranilde@gmail.com
Ⓘⓓ https://orcid.org/0000-0003-2266-9023
Himanshu Verma
✉ vhimanshu975@gmail.com
Ⓘⓓ https://orcid.org/0000-0003-2373-8940
Om Silakari
✉ omsilakari@gmail.com
Ⓘⓓ https://orcid.org/0000-0002-8314-7395
Bhaskar Biswas
✉ bhaskarbiswas@nbu.ac.in
Ⓘⓓ https://orcid.org/0000-0002-5447-9729

References

[1]. Behera, B. C.; Mishra, R. R.; Thatoi, H. Recent biotechnological tools for diagnosis of corona virus disease: A review. *Biotechnol. Prog.* **2021**, *37*, e3078.
[2]. Kahn, J. S.; McIntosh, K. History and recent advances in Coronavirus discovery. *Pediatr. Infect. Dis. J.* **2005**, *24*, S223–S227.

[3]. Monto, A. S. Medical reviews. Coronaviruses. *Yale J. Biol. Med.* **1974**, *47*, 234–251.
[4]. Coelho, C.; Gallo, G.; Campos, C. B.; Hardy, L.; Würtele, M. Biochemical screening for SARS-CoV-2 main protease inhibitors. *PLoS One* **2020**, *15*, e0240079.
[5]. Yuan, Y.; Zhao, Y.-J.; Zhang, Q.-E.; Zhang, L.; Cheung, T.; Jackson, T.; Jiang, G.-Q.; Xiang, Y.-T. COVID-19-related stigma and its sociodemographic correlates: a comparative study. *Global. Health* **2021**, *17*, 54.
[6]. Pedersen, S. F.; Ho, Y.-C. SARS-CoV-2: a storm is raging. *J. Clin. Invest.* **2020**, *130*, 2202–2205.
[7]. Huang, C.; Wang, Y.; Li, X.; Ren, L.; Zhao, J.; Hu, Y.; Zhang, L.; Fan, G.; Xu, J.; Gu, X.; Cheng, Z.; Yu, T.; Xia, J.; Wei, Y.; Wu, W.; Xie, X.; Yin, W.; Li, H.; Liu, M.; Xiao, Y.; Gao, H.; Guo, L.; Xie, J.; Wang, G.; Jiang, R.; Gao, Z.; Jin, Q.; Wang, J.; Cao, B. Clinical features of patients infected with 2019 novel coronavirus in Wuhan, China. *Lancet* **2020**, *395*, 497–506.
[8]. Li, R.; Pei, S.; Chen, B.; Song, Y.; Zhang, T.; Yang, W.; Shaman, J. Substantial undocumented infection facilitates the rapid dissemination of novel coronavirus (SARS-CoV-2). *Science* **2020**, *368*, 489–493.
[9]. Peiris, J. S. M.; Yuen, K. Y.; Osterhaus, A. D. M. E.; Stöhr, K. The severe acute respiratory syndrome. *N. Engl. J. Med.* **2003**, *349*, 2431–2441.
[10]. Wang, F.; Hou, H.; Luo, Y.; Tang, G.; Wu, S.; Huang, M.; Liu, W.; Zhu, Y.; Lin, Q.; Mao, L.; Fang, M.; Zhang, H.; Sun, Z. The laboratory tests and host immunity of COVID-19 patients with different severity of illness. *JCI Insight* **2020**, *5*, e137799.
[11]. Yan, R.; Zhang, Y.; Li, Y.; Xia, L.; Guo, Y.; Zhou, Q. Structural basis for the recognition of SARS-CoV-2 by full-length human ACE2. *Science* **2020**, *367*, 1444–1448.
[12]. Hadjadj, J.; Yatim, N.; Barnabei, L.; Corneau, A.; Boussier, J.; Smith, N.; Péré, H.; Charbit, B.; Bondet, V.; Chenevier-Gobeaux, C.; Breillat, P.; Carlier, N.; Gauzit, R.; Morbieu, C.; Pène, F.; Marin, N.; Roche, N.; Szwebel, T.-A.; Merkling, S. H.; Treluyer, J.-M.; Veyer, D.; Mouthon, L.; Blanc, C.; Tharaux, P.-L.; Rozenberg, F.; Fischer, A.; Duffy, D.; Rieux-Laucat, F.; Kernéis, S.; Terrier, B. Impaired type I interferon activity and inflammatory responses in severe COVID-19 patients. *Science* **2020**, *369*, 718–724.
[13]. Olagnier, D.; Farahani, E.; Thyrsted, J.; Blay-Cadanet, J.; Herengt, A.; Idorn, M.; Hait, A.; Hernaez, B.; Knudsen, A.; Iversen, M. B.; Schilling, M.; Jørgensen, S. E.; Thomsen, M.; Reinert, L. S.; Lappe, M.; Hoang, H.-D.; Gilchrist, V. H.; Hansen, A. L.; Ottosen, R.; Nielsen, C. G.; Møller, C.; van der Horst, D.; Peri, S.; Balachandran, S.; Huang, J.; Jakobsen, M.; Svenningsen, E. B.; Poulsen, T. B.; Bartsch, L.; Thielke, A. L.; Luo, Y.; Alain, T.; Rehwinkel, J.; Alcamí, A.; Hiscott, J.; Mogensen, T. H.; Paludan, S. R.; Holm, C. K. SARS-CoV2-mediated suppression of NRF2-signaling reveals potent antiviral and anti-inflammatory activity of 4-octyl-itaconate and dimethyl fumarate. *Nat. Commun.* **2020**, *11*, 4938.
[14]. Saichi, M.; Ladjemi, M. Z.; Korniotis, S.; Rousseau, C.; Ait Hamou, Z.; Massenet-Regad, L.; Amblard, E.; Noel, F.; Marie, Y.; Bouteiller, D.; Medvedovic, J.; Pène, F.; Soumelis, V. Single-cell RNA sequencing of blood antigen-presenting cells in severe COVID-19 reveals multi-process defects in antiviral immunity. *Nat. Cell Biol.* **2021**, *23*, 538–551.
[15]. Mahato, R. K.; Mahanty, A. K.; Kotakonda, M.; Prasad, S.; Bhattacharyya, S.; Biswas, B. A hydrated 2,3-diaminophenazinium chloride as a promising building block against SARS-CoV-2. *Sci. Rep.* **2021**, *11*, 23122.
[16]. Kobayashi, S.; Mori, Y.; Fossey, J. S.; Salter, M. M. Catalytic enantioselective formation of C–C bonds by addition to imines and hydrazones: A ten-year update. *Chem. Rev.* **2011**, *111*, 2626–2704.
[17]. Layer, R. W. The chemistry of imines. *Chem. Rev.* **1963**, *63*, 489–510.
[18]. Gnanaprakasam, B.; Zhang, J.; Milstein, D. Direct synthesis of imines from alcohols and amines with liberation of H2. *Angew. Chem. Int. Ed Engl.* **2010**, *49*, 1468–1471.
[19]. Cano, R.; Ramón, D. J.; Yus, M. Transition-metal-free *O*-, *S*-, and *N*-arylation of alcohols, thiols, amides, amines, and related heterocycles. *J. Org. Chem.* **2011**, *76*, 654–660.
[20]. Chen, B.; Wang, L.; Gao, S. Recent advances in aerobic oxidation of alcohols and amines to imines. *ACS Catal.* **2015**, *5*, 5851–5876.
[21]. Wang, J.; Lu, S.; Cao, X.; Gu, H. Common metal of copper(0) as an efficient catalyst for preparation of nitriles and imines by controlling additives. *Chem. Commun. (Camb.)* **2014**, *50*, 5637–3640.
[22]. Sonobe, T.; Oisaki, K.; Kanai, M. Catalytic aerobic production of imines en route to mild, green, and concise derivatizations of amines. *Chem. Sci.* **2012**, *3*, 3249–3255.
[23]. Mudi, P. K.; Mahato, R. K.; Joshi, M.; Shit, M.; Choudhury, A. R.; Das, H. S.; Biswas, B. Copper(II) complexes with a benzimidazole functionalized Schiff base: Synthesis, crystal structures, and role of ancillary ions in phenoxazinone synthase activity. *Appl. Organomet. Chem.* **2021**, *35*, e6211.
[24]. Mudi, P. K.; Mahanty, A. K.; Kotakonda, M.; Prasad, S.; Bhattacharyya, S.; Biswas, B. A benzimidazole scaffold as a promising inhibitor against SARS-CoV-2. *J. Biomol. Struct. Dyn.* **2023**, *41*, 1798–1810.
[25]. Mudi, P. K.; Mahato, R. K.; Verma, H.; Panda, S. J.; Purohit, C. S.; Silakari, O.; Biswas, B. In silico anti-SARS-CoV-2 activities of five-membered

heterocycle-substituted benzimidazoles. *J. Mol. Struct.* **2022**, *1261*, 132869.

[26]. Bruker (2009). SMART (Version 5.0) and SAINT (Version 6.02). Bruker AXS Inc., Madison, Wisconsin, USA.

[27]. Sheldrick, G. M. (1996). SADABS. University of Göttingen, Germany.

[28]. Sheldrick, G. M. (1996). SHELXS97 and SHELXL97. University of Göttingen, Germany.

[29]. Dolomanov, O. V.; Bourhis, L. J.; Gildea, R. J.; Howard, J. A. K.; Puschmann, H. *OLEX2*: a complete structure solution, refinement and analysis program. *J. Appl. Crystallogr.* **2009**, *42*, 339–341.

[30]. Zhang, D.; Hamdoun, S.; Chen, R.; Yang, L.; Ip, C. K.; Qu, Y.; Li, R.; Jiang, H.; Yang, Z.; Chung, S. K.; Liu, L.; Wong, V. K. W. Identification of natural compounds as SARS-CoV-2 entry inhibitors by molecular docking-based virtual screening with bio-layer interferometry. *Pharmacol. Res.* **2021**, *172*, 105820.

[31]. Yi, Y.; Li, J.; Lai, X.; Zhang, M.; Kuang, Y.; Bao, Y.-O.; Yu, R.; Hong, W.; Muturi, E.; Xue, H.; Wei, H.; Li, T.; Zhuang, H.; Qiao, X.; Xiang, K.; Yang, H.; Ye, M. Natural triterpenoids from licorice potently inhibit SARS-CoV-2 infection. *J. Adv. Res.* **2022**, *36*, 201–210.

[32]. Ma, J.; Chen, Y.; Wu, W.; Chen, Z. Structure and function of N-terminal zinc finger domain of SARS-CoV-2 NSP2. *Virol. Sin.* **2021**, *36*, 1104–1112.

[33]. Thuy, B. T. P.; My, T. T. A.; Hai, N. T. T.; Hieu, L. T.; Hoa, T. T.; Thi Phuong Loan, H.; Triet, N. T.; Van Anh, T. T.; Quy, P. T.; Van Tat, P.; Van Hue, N.; Quang, D. T.; Trung, N. T.; Tung, V. T.; Huynh, L. K.; Nhung, N. T. A. Investigation into SARS-CoV-2 resistance of compounds in garlic essential oil. *ACS Omega* **2020**, *5*, 8312–8320.

[34]. Bauer, M. R.; Mackey, M. D. Electrostatic complementarity as a fast and effective tool to optimize binding and selectivity of protein–ligand complexes. *J. Med. Chem.* **2019**, *62*, 3036–3050.

[35]. Du, X.; Li, Y.; Xia, Y.-L.; Ai, S.-M.; Liang, J.; Sang, P.; Ji, X.-L.; Liu, S.-Q. Insights into protein–ligand interactions: Mechanisms, models, and methods. *Int. J. Mol. Sci.* **2016**, *17*, 144.

[36]. He, X.; Man, V. H.; Yang, W.; Lee, T.-S.; Wang, J. A fast and high-quality charge model for the next generation general AMBER force field. *J. Chem. Phys.* **2020**, *153*, 114502.

[37]. Jakalian, A.; Bush, B. L.; Jack, D. B.; Bayly, C. I. Fast, efficient generation of high-quality atomic charges. AM1-BCC model: I. Method. *J. Comput. Chem.* **2000**, *21*, 132–146.

[38]. Kelly, B. D.; Smith, W. R. A simple method for including polarization effects in solvation free energy calculations when using fixed-charge force fields: Alchemically polarized charges. *ACS Omega* **2020**, *5*, 17170–17181.

[39]. Eastman, P.; Swails, J.; Chodera, J. D.; McGibbon, R. T.; Zhao, Y.; Beauchamp, K. A.; Wang, L.-P.; Simmonett, A. C.; Harrigan, M. P.; Stern, C. D.; Wiewiora, R. P.; Brooks, B. R.; Pande, V. S. OpenMM 7: Rapid development of high performance algorithms for molecular dynamics. *PLoS Comput. Biol.* **2017**, *13*, e1005659.

[40]. Frisch, M. J.; Trucks, G. W.; Schlegel, H. B.; Scuseria, G. E.; Robb, M. A.; Cheeseman, J. R.; Montgomery, J. A.; Vreven, T.; Kudin, K. N.; Burant, J. C.; Millam, J. M.; Iyengar, S. S.; Tomasi, J.; Barone, V.; Mennucci, B.; Cossi, M.; Scalmani, G.; Rega, N.; Petersson, G. A.; Nakatsuji, H.; Hada, M.; Ehara, M.; Toyota, K.; Fukuda, R.; Hasegawa, J.; Ishida, M.; Nakajima, T.; Honda, Y.; Kitao, O.; Nakai, H.; Klene, M.; Li, X.; Knox, J. E.; Hratchian, H. P.; Cross, J. B.; Adamo, C.; Jaramillo, J.; Gomperts, R.; Stratmann, R. E.; Yazyev, O.; Austin, A. J.; Cammi, R.; Pomelli, C.; Ochterski, J. W.; Ayala, P. Y.; Morokuma, K.; Voth, G. A.; Salvador, P.; Dannenberg, J. J.; Zakrzewski, V. G.; Dapprich, S.; Daniels, A. D.; Strain, M. C.; Farkas, O.; Malick, D. K.; Rabuck, A. D.; Raghavachari, K; Foresman, J. B.; Ortiz, J. V.; Cui, Q.; Baboul, A. G.; Clifford, S.; Cioslowski, J.; Stefanov, B. B.; Liu, G.; Liashenko, A.; Piskorz, P.; Komaromi, I.; Martin, R. L.; Fox, D. J.; Keith, T.; Al-Laham, M. A.; Peng, C. Y.; Nanayakkara, A.; Challacombe, M.; Gill, P. M. W.; Johnson, B.; Chen, W.; Wong, M. W.; Gonzalez, C.; Pople, J. A. Gaussian 09 (Revision A.02), Gaussian, Inc., Wallingford CT, 2009.

[41]. Zhao, Y.; Truhlar, D. G. A new local density functional for main-group thermochemistry, transition metal bonding, thermochemical kinetics, and noncovalent interactions. *J. Chem. Phys.* **2006**, *125*, 194101.

[42]. De, A.; Sahu, A.; Paul, S.; Joshi, M.; Choudhury, A. R.; Biswas, B. Structural and luminescent properties of a new 1D Cadmium(II) coordination polymer: A combined effort with experiment & theory. *J. Mol. Struct.* **2018**, *1167*, 187–193.

[43]. Roy, S.; Paul, P.; Karar, M.; Joshi, M.; Paul, S.; Choudhury, A. R.; Biswas, B. Cascade detection of fluoride and bisulphate ions by newly developed hydrazine functionalised Schiff bases. *J. Mol. Liq.* **2021**, *326*, 115293.

[44]. Mahato, S.; Meheta, N.; Kotakonda, M.; Joshi, M.; Shit, M.; Choudhury, A. R.; Biswas, B. Synthesis, structure, polyphenol oxidase mimicking and bactericidal activity of a zinc-schiff base complex. *Polyhedron* **2021**, *194*, 114933.

[45]. Rajani, K. M.; Prafullya, K. M.; Mayukh, D.; Bhaskar, B. A direct metal-free synthetic approach for the efficient production of privileged benzimidazoles in water medium under aerobic condition. *Asian J. Org. Chem.* **2021**, *10*, 2954–2963.

[46]. Culletta, G.; Gulotta, M. R.; Perricone, U.; Zappalà, M.; Almerico, A. M.; Tutone, M. Exploring the SARS-CoV-2 proteome in the search of potential inhibitors via structure-based pharmacophore modeling/docking approach. *Computation (Basel)* **2020**, *8*, 77.

[47]. Badavath, V. N.; Kumar, A.; Samanta, P. K.; Maji, S.; Das, A.; Blum, G.; Jha, A.; Sen, A. Determination of potential inhibitors based on isatin derivatives against SARS-CoV-2 main protease (mpro): a molecular docking, molecular dynamics and structure-activity relationship studies. *J. Biomol. Struct. Dyn.* **2022**, *40*, 3110–3128.

[48]. Purwati; Miatmoko, A.; Nasronudin; Hendrianto, E.; Karsari, D.; Dinaryanti, A.; Ertanti, N.; Ihsan, I. S.; Purnama, D. S.; Asmarawati, T. P.; Marfiani, E.; Yulistiani; Rosyid, A. N.; Wulaningrum, P. A.; Setiawan, H. W.; Siswanto, I.; Tri Puspaningsih, N. N. An in vitro study of dual drug combinations of anti-viral agents, antibiotics, and/or hydroxychloroquine against the SARS-CoV-2 virus isolated from hospitalized patients in Surabaya, Indonesia. *PLoS One* **2021**, *16*, e0252302.